Mimicking cochlear pre-processing using critically coupled MEMS sensors

NEUROMORPHIC
Computing and Engineering

OPEN ACCESS

RECEIVED
18 November 2025

REVISED
26 January 2026

ACCEPTED FOR PUBLICATION
13 February 2026

PUBLISHED
25 February 2026

PAPER

Mimicking cochlear pre-processing using critically coupled MEMS sensors

Kalpan Ved[1,6,*], **Hermann Folke Johann Rolf**[2,6], **Tzvetan Ivanov**[3], **Thomas Meurer**[4], **Martin Ziegler**[5] and **Claudia Lenk**[1]

[1] Department of Biomedical Sensor Systems and Microsystems, University Ulm, Ulm, Germany
[2] Automation and Control Group, Department of Electrical and Information Engineering, Faculty of Engineering, Kiel University, Kiel, Germany
[3] Micro- and Nanoelectronic Systems, Institute of Micro- and Nanotechnologies (IMN) MacroNano®, Technische Universität Ilmenau, Ilmenau, Germany
[4] Digital Process Engineering Group, Institute of Mechanical Process Engineering and Mechanics (MVM), Karlsruhe Institute of Technology, Karlsruhe, Germany
[5] Energy Materials and Devices, Department of Materials Science, Faculty of Engineering, Kiel University, Kiel, Germany
[6] These authors contributed equally to this work.
[*] Author to whom any correspondence should be addressed.

E-mail: kalpan.ved@uni-ulm.de

Keywords: compressive nonlinearity, critical oscillators, Andronov–Hopf bifurcation, neuromorphic acoustic sensing, frequency tunability

Supplementary material for this article is available online

Abstract

The characteristic of our hearing is essentially based on the mechanics in our inner ear. Around 3000 hair cells in the cochlea decode vibrations into electrical signals, covering frequencies from 0.020–20 kHz with relative resolutions normalized by their natural frequency of 0.1%–0.4% and a high dynamic range of 0–120 dB. These dynamic properties can be described by critical oscillators as they provide high resolution and nonlinear response near their critical points. However, the wide frequency range cannot be achieved as high sensitivity requires high Q-factors and is therefore associated with narrow frequency range. To overcome this, frequency tunability could be used to increase the detectable frequency range while maintaining high sensitivity. One solution to achieve frequency tuning is the mutual coupling of oscillators. To this end, a bio-inspired sensing system based on coupled resonators tuned near their critical points is presented, whose frequency can be tuned by varying the feedback of the individual resonator. In the coupled system three Andronov–Hopf bifurcations are identified, where two of them enable frequency tunability. We show that this adaptability of the frequency enables the coverage of a wide frequency range with limited number of resonators and yet preserves a high resolution with low number of resonators, which make them suitable for hardware implementation.

1. Introduction

Even though technological speech processing is rapidly improving by applying deep neural networks and nonlinearities in the pre-processing stage [1–3], the sound perception of mammals has much better performance in terms of energy efficiency, hearing comprehension and susceptibility to errors. For instance, state of the art speech processing fails in noisy environments, whereas human sound perception of a specific source in noisy environments works efficiently [4]. This property of sound perception is called cocktail party effect [5, 6], which is achieved by tuning hearing properties depending on the input and the hearing environment. In biological systems, pre-processing of sound signals takes place already in the cochlea, i.e. the sound sensor, and it is constantly tuned. This integration and tuning are compared to technological systems to yield better performance, especially regarding noisy environments. To overcome the limitations of technological systems, several bio-inspired sensors and neuromorphic implementations

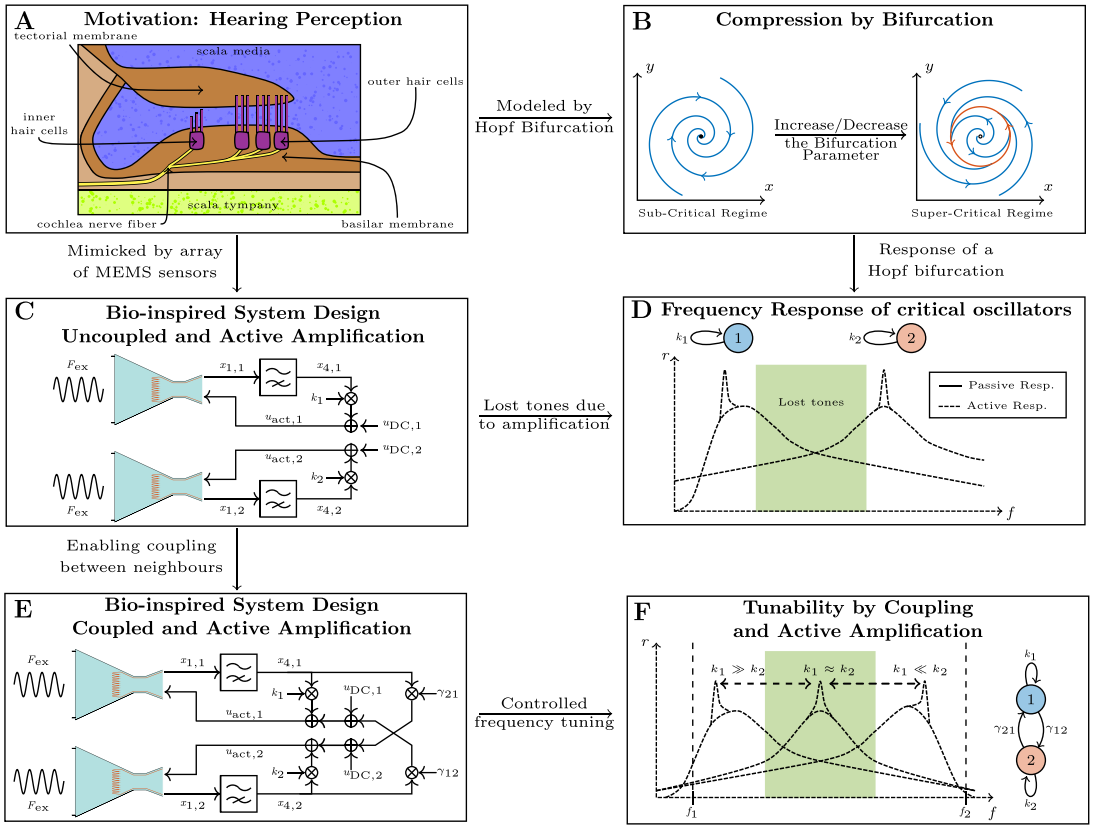

Figure 1. The organ of corti can be modeled by many critical resonators tuned near their Andronov–Hopf bifurcation point and can be mimicked by a MEMS system comprised of an array of MEMS resonators. (A) Sketch of the anatomy of the organ of corti. (B) After the bifurcation parameter surpasses the critical point of an Andronov–Hopf bifurcation, a limit cycle emerges in a system. This regime is called super-critical. In contrast to this, this system is asymptotically stable when the critical point is not surpassed. This regime is referred as sub-critical. For acoustic sensing, the sub-critical regime is beneficial as a compressive nonlinearity can be tuned by assigning the bifurcation parameter correctly. (C) Setup of two uncoupled MEMS resonators. A feedback loop is obtained by amplifying the high pass filtered MEMS's output by a factor k and introducing an offset DC voltage u_{DC}. This system acts as a critical oscillator, where k_i is the bifurcation parameter. (D) These MEMS resonators are critically tuned near the critical point, hence giving sharp active response at the characteristic frequency. Such sharp active response poses a problem of lost sound tones between the resonators. (E) Coupling mechanism is enabled between neighboring MEMS resonators with close-by characteristic frequency to resolve this problem. Here, additional to feedback control, the high pass filtered signal from the ith MEMS resonator is amplified by coupling strength γ_{ji} and it is fed into the actuation of the jth MEMS resonator and vice versa. (F) Enabling coupling between these critically tuned MEMS resonators can enable frequency tuning of MEMS resonators, thus solving the problem of lost tones. It can be shown that this frequency tuning is an intrinsic property of coupled Andronov–Hopf oscillators tuned near a critical point of an Andronov–Hopf bifurcation.

of cochlear processing have been developed in recent years [7–13]. These integrate cochlear processing into or close to the sensor.

The two main pre-processing steps are frequency decomposition and nonlinear amplification of the signals, which are also the first steps in almost any technological sound recognition and analysis system [2]. It was shown that both are important to achieve a good performance in sound recognition tasks, see e.g. [1]. Frequency decomposition can be used to recognize a specific sound or sound source, since different sounds differ by their frequency components over time and thus the pattern of active frequencies is like a finger print of the sound. The nonlinear amplification is compressive in nature, so that strong signals are attenuated and weak signals are amplified [14–23] and redundancy is introduced into the measured signal [24]. Thereby, the amplification is dynamically tuned separately for each frequency band, which yields a better signal quality in changing and noisy environments.

These pre-processing properties are attributed to the interplay between the different parts of the organ of corti (see figure 1(A)), where sound sensing takes place in the cochlea.

Various attempts have been made to model the internal mechanism of the cochlea. Here, two different approaches can be distinguished, namely the filter bank approach and critical oscillator theory. In the filter bank approach cochlear processing is modeled in the form of parallel filter banks [25] or cascaded filter banks [26, 27]. They were developed to describe psychoacoustic experiments, such as detection of tones in noise maskers, as well as the frequency decomposition by the basilar membrane. The

initial filter bank models were linear. To model the nonlinear amplification typically automatic gain control is incorporated. Furthermore, additional nonlinearities between the filter stages can be incorporated to model also distortion effects, observed in human hearing [28]. In the second approach, the critical oscillator theory, nonlinearity and frequency filtering are achieved by one system, i.e. the critical oscillator. This theory hypothesizes that the cochlea consists of many critical oscillators operating near the critical point of an Andronov–Hopf bifurcation [21, 29] due to the resemblence of the cochlear dynamics to the dynamical behavior of a critical oscillator in the sub-critical regime of the Andronov–Hopf bifurcation. In this regime the response of a harmonically excited resonator close to its critical point is compresssively nonlinear and frequency selective [21, 30–35]. This reflects the small-signal amplification of the basilar membrane [36]. Regarding frequency decomposition, resonance (phase locking) of the critical oscillator to the input acoustic signal is assumed. Here, the question arises, how the coverage of the auditory frequency range can be achieved despite the high quality factors of critical oscillators. Due to the sharp responses, not all tones might be sensed/recorded (see figure 1(D)) and a large number of resonators would be required to achieve the 0.4% relative frequency resolution, much more than the approximately 3000 inner hair cells in the cochlea [37, chapter 9].

To address this, coupling of critical oscillators is discussed. Possible physical coupling mechanisms in the cochlea are coupling by the tectorial membrane, the fluid between the hair cells and extracellular linkages [38–42]. Theoretical analysis by Gomez *et al* showed that an Andronov–Hopf bifurcation is preserved in two coupled Andronov–Hopf oscillators, such that both oscillators exhibit a common characteristic frequency and this system can also be viewed as a critical oscillator [34]. Dierkes *et al* modeled clusters of neighboring hair cell bundles as system of coupled Andronov–Hopf oscillators and observed sensitivity enhancement [43]. Furthermore, coupling of a larger number of critical oscillators was shown to yield clusters of oscillators with similar frequencies. This effect is discussed as underlying mechanism for spontaneous oto-acoustic emissions [44–46]. Coupling was also shown to reduce the effect of noise and increase the sensitivity [42].

Coupled, critical oscillators can be realized in various approaches. Here, three approaches are discussed. First, an array of critical oscillators can be implemented by metamaterials, i.e. synthetic materials whose properties drastically differ from natural materials, to build frequency-selective structures [8]. For this, the frequency decomposition can be mimicked by building frequency-selective structures with these materials by, e.g. combining metamaterials and sub-wavelength resonators [8–10] or designing the geometry of the metamaterial similar to the cochlea [11]. The nonlinear amplification is, e.g. induced by feeding back the frequency component of each resonator into the sensor [9]. Second, a combination of a microphone and a cochlear amplifier can be employed to mimic cochlear processing [12, 13]. Here, the sound is converted into an electric signal and the transduced signal is processed by, e.g. an integrated circuit [12] or in-materia computing units such as the combination of dopant network processing units and an in-memory computing chip consisting of memristive devices [13]. Third, the critical oscillators can be directly implemented by utilizing microelectromechanical system (MEMS) sensors. This system is based on our recently developed neuromorphic (bio-inspired) acoustic sensor [7] and acts as sound-driven resonators in connection with an electronic feedback (see figure 1(C)). It is shown in [7, 47, 48] that this system has a compressive and frequency-selective response (see figure 1(D)), which can be described by a controllable Andronov–Hopf bifurcation. Here we study the coupling of these critical oscillators in both an experimental system and the associated theoretical analysis. Coupling is realized by feeding the output signals to the actuator of the neighboring sensor (see figure 1(E)). Besides the above discussed sensitivity enhancement and common center frequency due to coupling, we observe that this common frequency can be tuned by changing the feedback strength [49]. This is visualized in figure 1(F). As the feedback strength can also be used to control an Andronov–Hopf bifurcations, it can be used to modify the bandwidth of the MEMS resonators, so that the adjustment of the feedback strengths of the two sensors can be interpreted as changing the asymmetry between the quality factors of the individual resonator. This helps to resolve the problem of lost tones [50] and might be a mechanism realized in the cochlea, controlled, e.g. by efferent feedback. In contrast to our approach, conventional methods to enable frequency tunability are based on changing the geometry of the MEMS sensor, so that a nonlinear strain-stress relationship arises and the characteristic frequency becomes dependent on the deflection [51–53]. It can be shown that by closing the feedback loop of these MEMS sensors, the Andronov–Hopf bifurcation is preserved [53]. However, the sound will be distorted as it is frequency modulated with itself [52, 53].

In the next section, the system is briefly explained, before results on the frequency tunability and the different operation regimes are shown. This is followed by comparing the measured critical points

with the critical points derived in [49][7]. In addition, a sensitivity analysis in the sub-critical regime is performed to characterize the compressive nonlinearity. Finally, some remarks conclude the paper.

2. System description

Figure 1(E) shows the setup of two MEMS resonators with the feedback and coupling scheme. Each MEMS resonator is a silicon beam, which can be thermomechanically actuated using the bimorph effect and whose deflection is measured by a piezo-resistive Wheatstone bridge [7, 48]. The resonators have a fixed natural frequency depending on the material constants and the geometry, i.e. length, width, and thickness [55, example 6.7] [56]. If the resonators are excited by sound, they act as band-pass filters due to resonance, enabling frequency decomposition of the sound signal. Details about the experimental and simulation setup and the parameters are given in appendices A–C. In addition, the experimental investigations are compared to the analysis on the dynamic model of the coupled system performed in [49]. The analysis is briefly summarized in appendix D.

As the MEMS is modeled by an Euler–Bernoulli beam with linear strain, feedback is applied to obtain nonlinear dynamics for the sensors. Therefore, an actuation signal is created with a bias voltage and a part depending on the sensor's output. As shown in figure 1(E), there are two feedback mechanisms implemented for each sensor (with an additional bias voltage for actuation): (i) self-feedback governed by feedback strengths k_1, k_2. Here the sensing signal of one resonator is multiplied with a factor k_i for all $i = 1, 2$ and is fed back in the actuation of the same resonator. By increasing this feedback parameter k_i above a certain threshold, the system goes into Andronov–Hopf bifurcation, indicated in the experiment by the onset of autonomous oscillations, whose frequency is approximately the natural frequency of the resonator. This critical point is called feedback critical point and is denoted as $k^*_{i,j}$ for all $i, j = 1, 2$. (ii) The second mechanism is cross-coupling governed by coupling strengths γ_{12}, γ_{21}. Here the sensing signal of the ith resonator is multiplied with the coupling strength γ_{ij} and is fed into the actuation of the jth resonator. While, the ith resonator is actuated by the sensing signal of the jth resonator, which is multiplied by the coupling strength γ_{ji}. By increasing the product between the coupling strength $\gamma_{12}\gamma_{21} \in \mathbb{R}$ beyond a certain threshold, the system of coupled resonators collectively undergoes Andronov–Hopf bifurcations [49], indicated by autonomous oscillations, whose natural frequency is different to the natural frequency of the MEMS sensors. Hence, this bifurcation is different than the bifurcations induced by the feedback strength. Its critical point is termed as coupling critical point and is denoted as $\gamma^*_{12,j}\gamma^*_{21,j} \in \mathbb{R}$ for all $i, j = 1, 2, 3$.

It is important to note that to induce strong nonlinearities, coupled MEMS resonators have to be tuned just below the critical point. This tuning is defined as critical tuning. Both the control parameters (k_i, γ_{ij}) have different effects on the individual resonators. Their combination can yield new effects like the tunability of the systems frequency described in the next section.

3. Tuning of characteristic frequency

An important characteristics observed when combining coupling and self-feedback for two MEMS resonators is the tunability of their characteristic frequencies $f_{C,1}$ and $f_{C,2}$. Particularly, the characteristic frequencies $f_{C,1}$ and $f_{C,2}$ depend on the parameter set $\{k_1, k_2, \gamma_{12}, \gamma_{21}\}$ as these parameters can be used to control multiple Andronov–Hopf bifurcation. Here, the characteristic frequency of the coupled resonators is aligned by assigning the the coupling strength $\gamma_{12}\gamma_{21}$ in the neighborhood of the coupling critical point. This frequency is influenced by the damping (and thus the Q-factor) of the resonators. Hence, if the feedback strengths satisfy $k_1 = k_2 = 0$, the characteristic frequency of the coupled system is closer to the natural frequency of the MEMS sensors with the larger Q-factor. To tune this frequency, the Q-factor of the MEMS sensors are adjusted by exploiting the feedback strengths k_1 and k_2 as these parameters control a different Andronov–Hopf bifurcation. Hence, the Q-factor of one resonator is increased by moving closer to its feedback critical point. The frequency tunability is shown in figure 2. Here, the measured and the analytically predicted coupling critical point $\gamma^*_{12,1}\gamma^*_{21,1}$ and the frequency difference $\Delta f_{C,1} = f_{C,1} - f_1$ between the characteristic frequency $f_{C,1}$ of the tunable Andronov–Hopf bifurcation and the natural frequency f_1 are depicted as a function of the self-feedback strengths k_1 and k_1. The natural frequencies of the MEMS resonators are $f_1 = 3630$ Hz and $f_2 = 3790$ Hz and the feedback critical points are given by $k^*_{1,1} = 0.21875$ and $k^*_{2,1} = 0.1875$. To study frequency tunability,

[7] A brief summary of this bifurcation analysis is given in appendix D.

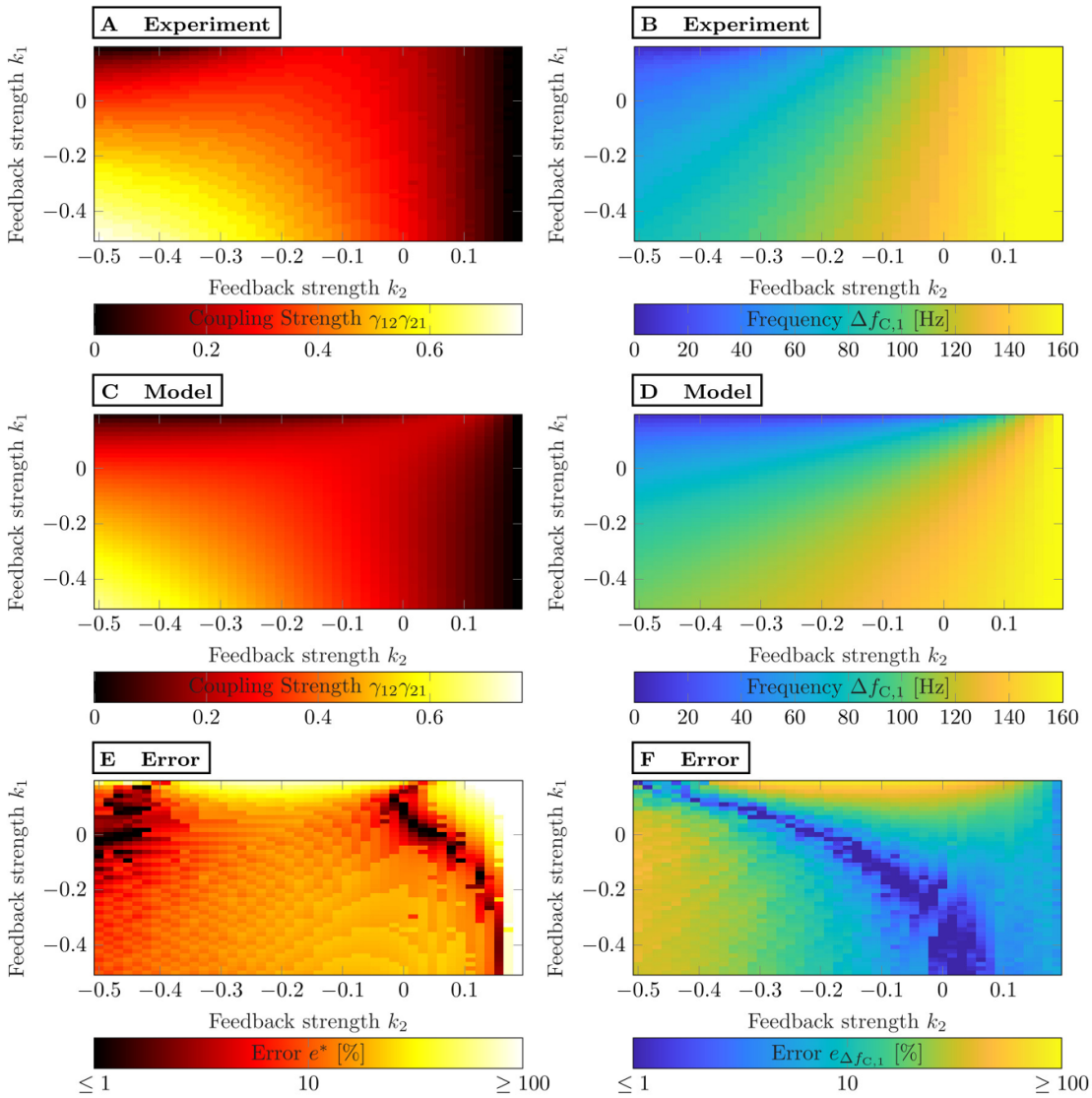

Figure 2. Comparison between the experimental and the theoretical results of frequency tunability close to the coupling critical point as a function of the feedback strengths $k_1 \in [-0.5, 0.1875]$ and $k_2 \in [-0.5, 0.1875]$ with a resolution of $0.015\,625 (= 1/64)$ for two MEMS sensors with $f_1 = 3630$ Hz, $f_2 = 3790$ Hz, and $u_{DC,1} = u_{DC,2} = -150$ mV. To enable the frequency tunability the coupling strength $\gamma_{12}\gamma_{21}$ is changed, so that the system remains in the nonlinear regime near the critical point and the characteristic frequency of both resonators aligns to a common characteristic frequency. The controllable shift in this aligned characteristic frequency is caused by controlling the feedback strengths of the resonators. This will change the bandwidth and the damping of the oscillators, since the feedback strengths induce an Andronov–Hopf bifurcation. (A) Coupling strength $\gamma_{12}\gamma_{21}$ in terms of the feedback strength k_1 and k_2 to ensure that the system remains near the critical point. (B) Experimentally measured tunability of the the frequency difference $\Delta f_{C,1} = f_{C,1} - f_1$ between the characteristic frequency $f_{C,2} = \omega_{C,2}/(2\pi)$ of the tunable bifurcation and the natural frequency f_1 of the higher frequency MEMS sensor in the sub-critical regime when stimulated with sound. The response of the lower frequency MEMS sensor is similar (provided in supplementary materials). (C) and (D) Predicted critical coupling strength $\gamma^*_{12,1}\gamma^*_{21,1}$ and frequency difference $\Delta f_{C,1}$. (E),(F) Relative errors e^* and $e_{f_{C,1}}$ between the measured and predicted coupling strength and frequency difference. (Reproduced from [54]. CC BY 4.0.)

the self-feedback strengths were sampled in $k_1 \in [-0.5, 0.1875]$ and $k_2 \in [-0.5, 0.1875]$ with a resolution of $0.015\,625 (= 1/64)$ and the DC-voltage is given by $u_{DC,1} = u_{DC,2} = -150$ mV. The critical point is determined by (i) setting the the feedback strengths k_1 and k_2 to a desired value and (ii) increasing the coupling strengths γ_{12} and γ_{21} until both MEMS resonators undergo autonomous oscillation simultaneously and are insensitive to sound stimulus. Second, the system of two coupled MEMS resonator is tuned below the critical point $\gamma^*_{12,1}\gamma^*_{21,1}$ in the nonlinear regime. For this, the coupling strength is given by $\gamma_{12}\gamma_{21} = \gamma^*_{12,1}\gamma^*_{21,1} - 0.001$ to ensure that the system is not operated in autonomous oscillation. Here symmetric coupling is assigned, i.e. $\gamma_{12} = \gamma_{21}$. The figures 2(A) and C) show the coupling critical point $\gamma^*_{12,1}\gamma^*_{21,1}$ in dependence of the self-feedback strengths k_i, which is adjusted to tune the system close to the critical point for each set of (k_1, k_2). Thereby, the lower the feedback strengths k_1 and k_2, the higher the required coupling strength $\gamma_{12}\gamma_{21}$ to induce bifurcation in the system.

Table 1. Summary on the conditions for the different operation regimes.

Operation regime	Critical point	Sign-condition	Δf-condition
Frequency tunable regime 1	$\gamma^*_{12,1}\gamma^*_{21,1}$	$\mathrm{sign}(\gamma^*_{12,1}\gamma^*_{21,1}) > 0$	$\Delta f < 206$ Hz
Frequency tunable regime 2	$\gamma^*_{12,2}\gamma^*_{21,2}$	$\mathrm{sign}(\gamma^*_{12,2}\gamma^*_{21,2}) < 0$	$\Delta f \geqslant 0$ Hz
Untunable regime	$\gamma^*_{12,3}\gamma^*_{21,3}$	$\mathrm{sign}(\gamma^*_{12,3}\gamma^*_{21,3}) > 0$	$\Delta f > 206$ Hz

To obtain the characteristic frequencies $f_{\mathrm{C},1}$ and $f_{\mathrm{C},2}$, sound with frequency sweep and a constant amplitude is applied by a loudspeaker at each operating point. Then a frequency analysis is done and all the steps (setting feedback parameters and tuning coupling strength) are repeated for each combination of k_1 and k_2. To compare the experimentally obtained and simulated frequency response, the frequency difference $\Delta f_{\mathrm{C},1} = f_{\mathrm{C},1} - f_1$ between the characteristic frequency $f_{\mathrm{C},1}$ of the tunable Andronov–Hopf bifurcation and the natural frequency f_1 are evaluated in dependence of the self-feedback strengths k_i, as this enables a more precise error analysis. The results are visualized in figures 2(B) and (D). Since coupling yields an alignment of the resonators to a common center frequency, the frequency color map of the second resonator $f_1 = 3630$ Hz resonator is similar and provided in Supplementary Materials.

The relative error e^* between the predicted and measured critical coupling strength and the relative error $e_{\Delta f_{\mathrm{C},1}}$ between the predicted and measured characteristic frequency are visualized in figures 2(E) and (F). These errors are computed by taking the absolute value of the error and dividing the result by the measurements for each feedback strengths k_1 and k_2. It turns out that the mean and the standard deviation of these errors are $\bar{e}^* = 0.316$ and $\sigma_{e^*} = 2.064$ for the critical coupling strengths and $\bar{e}_{\Delta f_{\mathrm{C},1}} = 0.154\,05$ and $\sigma_{e_{\Delta f_{\mathrm{C},1}}} = 0.136\,42$ for the characteristic frequency. In particular, the large maximum $\max e^* = 62\,1362\,\%$ of the relative error of the critical coupling strength $\gamma^*_{12,1}\gamma^*_{12,1}$ is induced in the neighborhood of $k^*_{1,1}$ and $k^*_{2,1}$, where the critical coupling $\gamma^*_{12,1}\gamma^*_{12,1}$ is approximately zero. Hence, the measurement noise is amplified in this neighborhood. Neglecting these values results in mean $\bar{e}^* = 0.153$ and standard deviation $\sigma_{e^*} = 0.138$ of these errors for the critical coupling strengths.

As can be seen from figure 2 changing the feedback strengths k_1 and k_2 yields a shift of the characteristic frequencies, here in the range $[f_1, f_2]$. Since each of the resonators keeps a small bandwidth despite the tuning, this frequency tunability enables the coverage of the frequency range between characteristic frequencies with the dynamically adaptable feedback and coupling strength. To design a system with many MEMS resonators to cover the auditory frequency range and to design control loops for steering the frequency response, the pre-conditions and parameter dependency of the frequency tunability has to be known. This will be discussed in the next section.

4. Critical points

One of the pre-conditions that must be fulfilled to obtain frequency tunability is that the system behaves as a critical oscillator tuned in the neighborhood of the coupling critical point. The mathematical analysis of the system of coupled MEMS resonators yields three Andronov–Hopf bifurcations [49]. Thus, three operating regimes are possible. Experimentally, only one of the three bifurcation is dominant, i.e. a bifurcation is referred as dominant, if its critical point has the smallest magnitude, so that it is reached first. For measurements, the dominant bifurcation is of particular interest as the system goes into autonomous oscillations by crossing this critical point. In contrast to this, the other critical points cannot not be observed upon further increasing the bifurcation parameter. In particular, which of the three bifurcations of two coupled MEMS resonators is the dominant mainly depends on the natural frequencies of the coupled resonators and the polarity of the coupling strength. A summary on the conditions for a dominant critical point is given in table 1. To visualize this, the coupling critical points of two MEMS resonator are computed by increasing the natural frequency f of one sensor. For this, the parameters of the MEMS resonators are assumed to be identical for $f = 3630$ Hz. The results are visualized in figure 3(A). Here, the critical coupling strengths are depicted for each of the three critical points in dependence of the natural frequency of one of the two MEMS resonators and the frequency difference $\Delta f = |f_1 - f_2|$. The critical points 1 and 3 occur for positive coupling strengths while critical point 2 is observed for negative ones. In addition, the critical point 1 is dominant, if the frequency difference is small enough. Otherwise, the critical point 3 is dominant. For this example, the critical point 1 is observed up to a frequency difference of 206 Hz experimentally, while critical point 3 is observed for larger frequency differences. Following [49], this frequency difference is device-specific and it is dependent on the natural frequency, the Q-factor and the self-feedback strength of the MEMS resonators. A brief summary of the device-specific frequency difference is given in appendix D.

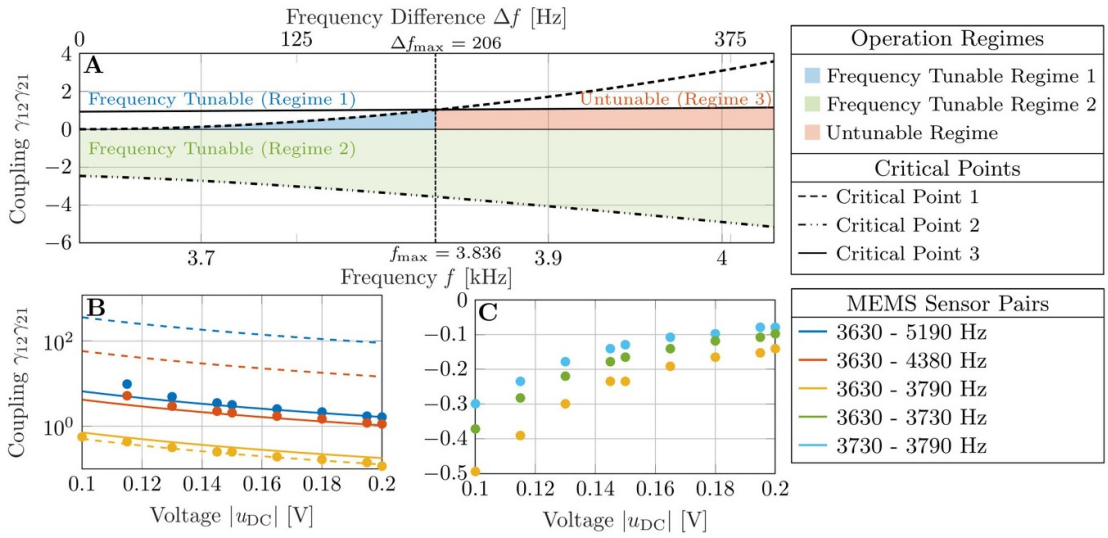

Figure 3. Coupling of MEMS resonators yields three different critical points depending on the frequency of coupled resonators and the polarity of coupling strength ($\gamma_{12}\gamma_{21}$) between the two resonators (A) MEMS system is tuned just below the coupling critical point to make it sensitive to the sound. This gives rise to three operation regimes. Set of resonators with frequency difference $\Delta f \leqslant 206$ Hz and positive coupling strength $\gamma_{12}\gamma_{21} < \gamma^*_{12,1}\gamma^*_{21,1}$ fall into frequency tunable regime 1 (shaded in blue) and critical point 1 (dashed curve) is the set of corresponding coupling critical points $\gamma^*_{12,1}\gamma^*_{21,1}$. Set of resonators with negative coupling strength $\gamma_{12}\gamma_{21} < 0$ and $|\gamma_{12}\gamma_{21}| < |\gamma^*_{12,2}\gamma^*_{21,2}|$ fall into frequency tunable regime 2 (shaded in green) and critical point 2 (dashed-dotted curve) is the set of corresponding coupling critical points $\gamma^*_{12,2}\gamma^*_{21,2}$. Set of resonators with frequency difference $\Delta f \geqslant 206$ Hz and positive coupling strength $\gamma_{12}\gamma_{21} > 0$ such that $\gamma_{12}\gamma_{21} < \gamma^*_{12,3}\gamma^*_{21,3}$ fall into untunable regime (shaded in red) and critical point 3 (solid curve) is the set of corresponding coupling critical points ($\gamma^*_{12,3}\gamma^*_{21,3}$). (B),(C) Theoretical prediction of critical points are depicted by lines, while measurements of critical points are marked by circles. (B) The critical points are plotted over $|u_{DC}|$ for set of resonators falling in frequency tunable regime 1 (3630–3790 Hz) and untunable Regime (3630–4380 Hz, 3630–5190 Hz). (C) Measurements of the critical point 2, i.e. frequency tunable regime 2, in terms of $|u_{DC}|$ for set of resonator pairs 4380–5190 Hz, 3630–3730 Hz and 3730–3790 Hz.

The critical coupling strength depends not only on the difference between the characteristic frequencies but also on the DC value of the feedback. The measured and predicted critical points for the three different bifurcations are shown in figures 3(B) and (C). Herein, experimental values of the critical points 1, 2 and, 3 are shown as dots, while the solid and dashed lines depict the respective analytical solutions for critical point 1 and 3. The different colors depict different pairs of coupled MEMS sensors. As can be seen from the measured and the computed critical points in terms of the DC-voltage u_{DC} in figures 3(B) and (C), increasing DC-voltage decreases the magnitude of the critical points to induce the required limit cycle. This is an effect of the used thermal actuation scheme, which depends on the applied power rather then the voltage itself. The DC-voltage u_{DC} plays an important role in imparting power into the system, requiring thus a smaller amount of coupling signal for larger DC values. It is demonstrated that theoretical and experimental results align qualitatively and quantitatively as visualized in figure 3(B). In contrast to this, critical point 2 is predicted by theory. However, the computed critical point is not matching the measurements quantitatively. (Note that reweighted, computed critical points are compared with the experimental results in the supplementary materials.) These observations might come from the fact that the MEMS resonators have to be described by coupled partial differential equations, while the considered MEMS model is derived by approximating the coupled PDEs with the Galerkin method [57], which is truncated after the first mode. Hence, by increasing the number of modes, the interaction between these modes will be captured, so that the quantitative behavior of the model might change.

5. Operation regimes for frequency tunability

The three operation regimes of the sensor system can be derived from the three critical points and exhibit different characteristics. For the analysis of the operation regimes, it is assumed that the DC-voltages are negative, i.e. $u_{DC,1}, u_{DC,2} < 0$. Here, the DC-voltages are given by $u_{DC,1} = u_{DC,2} = u_{DC} = -150$ mV. To observe the critical points of the different operation regimes, three scenarios are investigate(D) (i) MEMS sensors with the natural frequency $f_1 = 3630$ Hz and $f_2 = 3790$ Hz with $\gamma_{12}\gamma_{21} \geqslant 0$, (ii) MEMS sensors with the natural frequency $f_1 = 3630$ Hz and $f_2 = 3790$ Hz with $\gamma_{12}\gamma_{21} \leqslant 0$, and (iii)

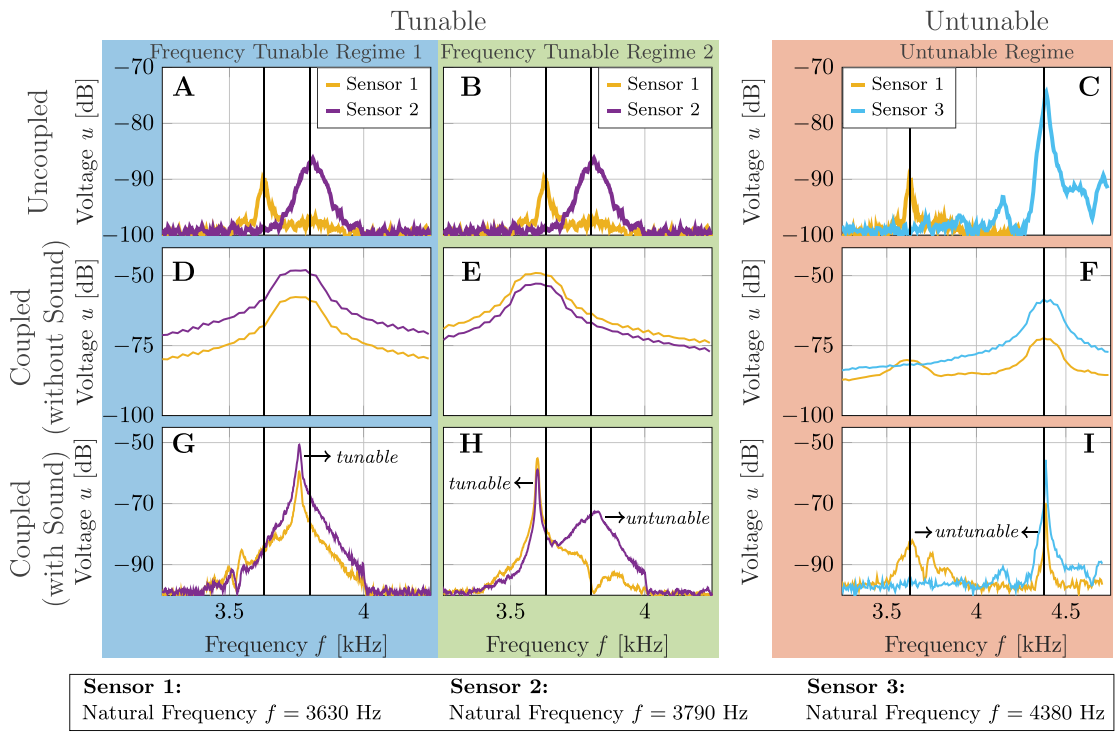

Figure 4. Different operation regimes and critical points. Three different sensors with natural characteristic frequency 3630 Hz, 3730 Hz and, 4380 Hz are coupled to present different regimes of operations. The critical points are given by $\gamma^*_{12,1}\gamma^*_{21,1} = 0.2658$, $\gamma^*_{12,2}\gamma^*_{21,2} = -0.234643$, and $\gamma^*_{12,3}\gamma^*_{21,3} = 3.062$. (A)–(C) Case of uncoupled resonators. All the sensors show response at their corresponding natural frequencies when excited with sound. (D)–(F) Coupled resonators in the super-critical regime. For this, the coupling bifurcation parameter $\gamma_{12}\gamma_{21}$ is increased beyond coupling critical point $\gamma^*_{12}\gamma^*_{21}$, so that the system of coupled resonators simultaneously undergoes self-oscillation without sound stimulus. (G)–(I) Coupled resonators in the sub-critical regime. Just below the critical point, i.e. $|\gamma_{12}\gamma_{21}| < |\gamma^*_{12,1}\gamma^*_{21,1}|$, yields enhanced sensitivity to sound. (G) Frequency response of sensors in frequency tunable regime 1 with $\gamma_{12}\gamma_{21} = 0.2346$. Frequency response depicts a tunable peak in the range $[f_1, f_2]$ where f_1 and f_2 are the natural characteristic frequencies of sensor 1 and 2 with $f_1 < f_2$. (H) Frequency response of sensors in frequency tunable regime 2 with $\gamma_{12}\gamma_{21} = -0.219$. Here two peaks are visible, one tunable and one untunable peak. The tunable peak can be approximately tuned within [79.6 Hz, f_1] [49]. Tuning in both the cases is done by changing the feedback parameter in $[k^*_{i,2}, k^*_{i,1}]$ for all $i = 1, 2$. I: Untunable Regime with $\gamma_{12}\gamma_{21} = 2.722$ where frequency tuning is not possible with coupling and feedback.

MEMS sensors with the natural frequency $f_1 = 3630$ Hz and $f_2 = 4380$ Hz with $\gamma_{12}\gamma_{21} \geqslant 0$. For all scenarios, the sensor response, i.e. magnitude of sensor voltage as a function of the frequency, is shown for (i) the uncoupled case ($\gamma_{12}\gamma_{21} = 0$) in the first row of figure 4, (ii) the supercritical case ($|\gamma_{12}\gamma_{21}| > \gamma^*_{12,i}\gamma^*_{21,i}$) in the middle row of figure 4, and (iii) the sub-critical regime ($0 < |\gamma_{12}\gamma_{21}| < |\gamma^*_{12,i}\gamma^*_{21,i}|$) in the bottom row of figure 4. For the cases uncoupled and sub-critical regime, sound input is provided using frequency sweep ranging from $3400 - 4000$ Hz, while for the super-critical regime no sound was applied. Tuning into the sub-critical regime is achieved by first obtaining the critical point $\gamma^*_{12}\gamma^*_{21}$, as described in section 3. Second, the coupling product $\gamma_{12}\gamma_{21}$ is set between 85%–95% of this critical value. For the specific regimes in this study, the parameters were chosen as follows: $\gamma_{12}\gamma_{21} = 0.2346$ for frequency-tunable regime 1, $\gamma_{12}\gamma_{21} = -0.219$ for frequency-tunable regime 2, and $\gamma_{12}\gamma_{21} = 2.722$ for the untunable regime. Magnitude voltage of sensor response [in dB] is calculated by the equation Voltage u [dB] $= 20\log_{10}(V/V_{\text{ref}})$. Here the reference voltage V_{ref} is 1 V. The results shown in figure 4 are explained in detail below. In addition, media files, which demonstrate these operation regimes, can be found in the Supplementary Material.

Frequency tunable regime 1: frequency tuning with positive coupling strength

The pre-condition is that the difference in natural frequencies $\Delta f = |f_1 - f_2|$ is smaller than a specific value and the product between the coupling strengths is positive, i.e. $\gamma_{12}\gamma_{21} > 0$. For the pair of MEMS sensors considered for figures 3 and 4, the values are $\Delta f < 206$ Hz with positive coupling strength $\gamma_{12}\gamma_{21} > 0$. Close to this critical point, the characteristic frequencies of both MEMS resonators align at one common center frequency $f_{C,1}$ in the super-critical regime (figure 4(D)) as well as in the sub-critical regime upon sound input (figure 4(G)). Moreover, the frequency of this harmonic oscillation can be tuned in the interval between the natural frequencies f_1 and f_2 by changing the feedback strengths k_1 and k_2.

Besides the alignment and tuning of characteristic frequencies in this operation regime, coupling increases the sensitivity of both sensors. In the uncoupled case (figure 4(A)), using two resonators with the natural frequencies (thick vertical lines) $f_1 = 3630\,\text{Hz}$ and $f_2 = 3790\,\text{Hz}$, the resonator with higher frequency has larger response amplitude ($-90\,\text{dB}$) than the lower frequency resonator ($-86\,\text{dB}$). Upon coupling in the sub-critical regime, the response of both resonators to a sound sweep shows a strong increase in amplitude by roughly 30 dB for both resonators i.e. $-86\,\text{dB}$ to $-50\,\text{dB}$ for high frequency resonator and $-90\,\text{dB}$ to $-60\,\text{dB}$ for low frequency resonator.

Frequency tunable regime 2: frequency tuning with negative coupling strength
This regime is shown in figures 4(B), (E) and (H) in the green column. The pre-condition for this regime is a negative coupling strength in the system, i.e. $\gamma_{12}\gamma_{21} < 0$. It occurs for all analyzed natural frequencies of the two resonators. Thereby, the higher the frequency, the larger the critical coupling strength. The frequency response in super-critical regime (i.e. after bifurcation) displays alignment of characteristic frequencies to a single peak (see figure 4(E)). Here, the characteristic frequency ($f_{C,1} \approx 3600\,\text{Hz}$) of the coupled system is below the lowest natural characteristic frequency of the coupled resonators, i.e. below $f_1 = 3630\,\text{Hz}$. In contrast to the amplitudes of the autonomous oscillations in Frequency Tunable Regime 1, the amplitude of autonomous oscillations is larger for the resonator with smaller natural frequency $f_1 = 3630\,\text{Hz}$ than the amplitude of the resonator with larger natural frequency $f_2 = 3790\,\text{Hz}$.

When the sensor is tuned just below the critical point and excited with sound sweep, two peaks are observed in the frequency response as shown in figure 4(H): a common peak for both resonators with a frequency lower than the lowest natural frequency of the resonators (similar to the super-critical regime) and one peak for the high-frequency resonator close to its natural frequency. The latter one cannot be tuned by changing the feedback strength whereas the common peak can be tuned in the frequency range $f_{C,2} \in [79.6\,\text{Hz}, f_1]$ by changing the feedback strengths k_1 and k_2. The lower boundary is given by the (maximum) characteristic frequencies of the Andronov–Hopf bifurcation, which is induced by the feedback strengths of the uncoupled MEMS resonators [49]. For the MEMS resonators with $f_1 = 3630\,\text{Hz}$ and $f_2 = 3790\,\text{Hz}$, the (numerically determined) characteristic frequencies read 61.6 Hz and 79.6 Hz. Again, coupling yields a stronger response to sound compared to the uncoupled case (roughly 20–30 dB larger). However, in comparison with the results from frequency tunable regime 1, the high-frequency resonator exhibits a 3 dB smaller response than in frequency tunable regime 1 but the low-frequency peak exhibits a 3 dB larger response as compared to frequency tunable regime 1. As the tunable peak moves away from natural characteristic frequencies of the resonators due to changing feedback strengths, its response amplitude decreases until it eventually vanishes in the noise level of $-100\,\text{dB}$.

Thus, polarity of coupling strength controls in which direction the common frequency peak can be shifted by changing the feedback strength and which resonator (high- or low-frequency) exhibits the stronger response.

Untunable regim(E) no frequency tuning
This regime is shown in figure 4 in the red column. The pre-condition for this regime is coupling MEMS resonator with large frequency difference $\Delta f = |f_1 - f_2| > 206\,\text{Hz}$ and positive coupling strength $\gamma_{12}\gamma_{21} > 0$. In this case, the frequency response of one resonator exhibits one peak at its characteristic frequency, whereas the response of the second resonator shows two peaks at the natural characteristic frequencies of both resonators in both, the super-critical regime as well as in the sub-critical regime (figure 4(F) and (I)). Here, the high frequency resonator has a stronger response than the low frequency resonator in all studied situations, i.e. uncoupled, super-critical and sub-critical. Thus, the occurrence of the second peak in the low-frequency resonator might be attributed by a driving of the low-frequency resonator by the high-frequency resonator. In contrast to this, the amplitude of the low-frequency resonator is too low to induce a response of the high-frequency resonator at the lower natural frequency. These peaks are untunable, i.e. they do not shift upon changing the feedback parameters k_1 and k_2. Nevertheless, the response amplitude of both resonators to sound is increased (by about 5–10 dB) when coupled, but this increase less than in the frequency tunable regime 1 and 2.

6. Sensitivity of the coupled MEMS sensors

Besides the frequency decomposition for sound sensing, the sensitivity is highly important. Oscillators tuned near the coupling critical point have a power law relationship between sensitivity and force, thus acting as small signal amplifier [33, 34, 43, 58–62]. The sensitivity of the coupled resonators is analyzed in regime 1, as it is the regime of interest due to its high sensitivity. Nevertheless, the overall dependence

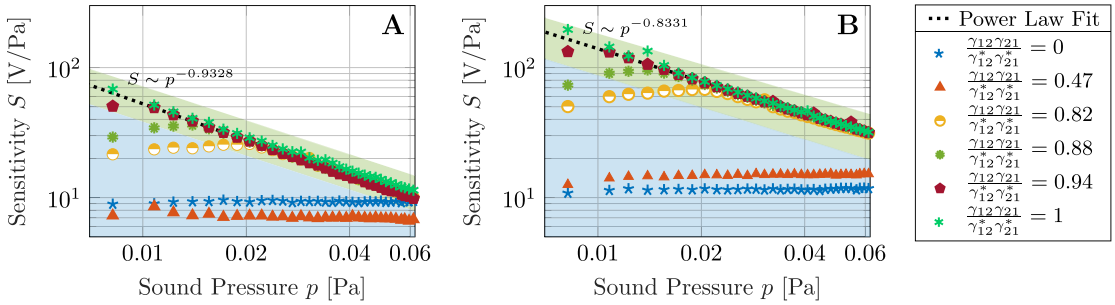

Figure 5. Sensitivity of the two coupled MEMS sensors in terms of the sound pressure. The natural frequencies of the coupled MEMS sensor are given by $f_1 = 3630$ Hz and $f_2 = 3790$ Hz. Here the bifurcation parameter $\gamma_{12}\gamma_{21}$ is varied from 0 to its critical point $\gamma_{12,1}^*\gamma_{21,1}^* = 0.2658$. (A) Sensitivity of the MEMS sensor with natural frequency $f_1 = 3630$ Hz. (B) Sensitivity of MEMS sensor with natural frequency $f_2 = 3790$ Hz. Here the blue shaded regime represents the linear regime and the green shaded region represents the nonlinear regime. Significant enhancement in sensitivity is observed for low sound pressures when tuned near the critical point.

of sensitivity on sound pressure should be similar for all regimes. For the sensitivity analysis, resonators with frequencies $f_1 = 3630$ Hz and $f_2 = 3790$ Hz, i.e. $\Delta f = |f_1 - f_2| < 206$ Hz, are coupled with $\gamma_{12}\gamma_{21} > 0$. The coupled system is stimulated by sound sweep from $3 - 4$ kHz with different intensities ranging from $0.003 - 0.06$ Pa and different coupling strengths are tested until the critical coupling strength. In addition, the DC-voltage is given by $u_{\mathrm{DC}} = -150$ mV. The sensitivity is then determined by measuring the amplitude response at resonance and dividing it by the sound pressure amplitude.

The sensitivity of the MEMS sensors with a natural frequency $f_1 = 3630$ Hz and $f_2 = 3790$ Hz are shown in figure 5. It is showcased that sensitivity is initially linear (for low coupling strengths) and increases with the coupling strength $\gamma_{12}\gamma_{21}$. When the bifurcation parameter approaches the critical point, i.e. $\gamma_{12,1}^*\gamma_{21,1}^* \approx 0.1329$, sensitivity becomes nonlinear and increases with decreasing sound pressure. A power law relationship can be observed between the sensitivity and sound pressure given by $S_1 = 3.013\,p^{-0.8331}$ (with RMSE of 2.214) and $S_2 = 0.718\,p^{-0.9328}$ (with RMSE of 0.3652) for sensor with natural frequencies $f_2 = 3790$ Hz and $f_1 = 3630$ Hz, respectively. The power law factors are in close agreement with the ones obtained by [43], where the modeling of coupled hair bundles showed an power law with exponent of -0.88. Here, the high-frequency resonator saturates at peak to peak voltage of 1.8 V for a sound pressure of 0.06 Pa, while the low-frequency resonator has not yet gone into saturation.

7. Discussion

It is showcased that each MEMS resonator acts as a band-pass filter, whose quality factor can be controlled by coupling two MEMS resonators. Hence, very fine tuning of the characteristic frequency can be achieved, if operated close to an Andronov–Hopf bifurcation. It is possible to modify the frequency for both resonators either in the range between both natural frequencies f_1 and f_2 using a positive coupling strength or between (approximately) $[79.6\,\mathrm{Hz}, f_1]$ with $f_1 < f_2$ for negative coupling strengths. Here, the feedback and the coupling strengths are just amplification factors, so that both can be varied fast and dynamically, even in large arrays of resonators.

Thereby, it is important that the resonators are operated as critical oscillators close to a critical point of an Andronov–Hopf bifurcation. For the considered system, three critical points can be distinguished, which depend on the natural frequencies of the resonators and the bias voltage in the feedback. These properties have been predicted by a mathematical model of the MEMS sensor. However, by using estimated parameters of the MEMS only critical point 1 and 3 can be computed, while the value of critical point 2 cannot be predicted. This issue can be explained by the fact that the utilized MEMS model is based on a dominant mode approximation of two coupled PDEs by employing the Galerkin method [57]. In particular, the considered MEMS model is derived by truncating the dominant mode approximation after the first mode. Hence, by increasing the number of modes, the interaction of other modes is captured, so that the quantitative behavior of the MEMS model will change.

Depending on the regime the system is operated in, different sensing properties are obtained. For MEMS resonators with a larger difference in natural frequencies, an operation regime is obtained, which does not allow for tuning the characteristic frequencies. Nevertheless, a connection between the two frequencies is obtained, which might be used for sound analysis and learning specific patterns. For smaller differences in natural frequencies, two more operation regimes are observed, for which frequency tuning

by changing feedback strength is possible, but the sensitivity to sound input differs for both. While for positive coupling strengths, the initially high-frequency sensor exhibits a higher response amplitude, for negative coupling strengths the initially low-frequency resonator exhibits the stronger response. In both cases, coupling yields a strong increase in sensitivity. Furthermore, a nonlinear dependence of sensitivity on sound pressure amplitude is obtained. The power law relationship is similar to the values obtained in the study of Dierkes *et al* [43] modeling coupled active hair cell bundles as Andronov–Hopf oscillators. This relationship clearly depicts the sensor as small signal amplifier, which aids in achieving wider dynamic ranges.

The ability to dynamically tune the characteristic frequencies of the critical oscillators has several advantages for a bio-inspired sound detection in neuromorphic hardware. First, due to the high quality factor, a large number of MEMS resonators are required to cover the audible frequency range. This means that the increase in the detectable frequency range due to the frequency tunability can be used to reduce the number of resonators required [50]. Second, tones occurring between the sharp characteristic peaks can be detected, which would be otherwise missed. Finally, the resonators characteristic frequency is set by their geometry and by their material parameters. Thus, the tunability of the frequency can be used to overcome mismatches due to fabrication tolerances. This phenomena of frequency tunability might also be present in the mammalian cochlea. The properties of sound sensing and the otoacoustic emission indicate a critical oscillator-like dynamics, whose dynamics are steered by efferent feedback (to the outer hair cells) [63, 64]. Thus, it might be interesting to analyze if tuning of the characteristic frequency occurs in mammalian hearing. A hint in this direction was given recently by Burwood *et al* [65], who showed that the place-coding of frequency in the cochlea is not as fixed as it was thought. Furthermore, dynamically tuning the frequency of the inner hair cells (as sensors) might be a mechanism to improve sound perception in noisy environments, since efferent feedback is discussed to be important in these situations.

Since coupling more sensors by this scheme increases the number of bifurcation points and, thus, the complexity for tuning the system, upscaling might require to use multiple pairs of coupled MEMS resonators, with no coupling between adjacent pairs. The resonator frequencies will be selected such that neighboring, decoupled sensor pairs have a minimal frequency gap, thereby minimizing tonal loss. Within each coupled pair, feedback and coupling parameters need to be tuned to independently adjust the frequency, bandwidth, and gain.

8. Conclusions

In this research work, we have analyzed an acoustic sensor consisting of two MEMS resonators, which can mimic the pre-processing properties of mammalian cochlea, mainly frequency decomposition and nonlinear compressive amplification. This dynamic behavior is induced by operating the system in the neighborhood of a critical point of an Andronov–Hopf bifurcation. For two coupled MEMS resonators, three different Andronov–Hopf bifurcations can be identified. These are characterized by their frequency tunability and their critical points. In particular, two Andronov–Hopf bifurcations exhibit a tunable characteristic frequency, while the characteristic frequency of the last Andronov–Hopf bifurcation cannot be modified. These bifurcations are dependent on the sign of the product between the coupling strength and the difference between the natural frequencies of the MEMS resonators. Here, the untunable regime is obtained by coupling MEMS with a large frequency difference and utilizing a positive product between the coupling strengths. Otherwise, the system has a tunable characteristic frequency.

Acknowledgment

Funded by the Deutsche Forschungsgemeinschaft (DFG, German Research Foundation) - Project-ID 434434223 - SFB 1461.

Data and code availability statement

The data that support the findings of this study are openly available at the following URL/DOI: https://doi.org/10.5281/zenodo.18336535 [70].

Setup and Freq. tuning plots available at https://doi.org/10.1088/2634-4386/ae45c9/data1.
Tunable regime 1- MEMS 1 available at https://doi.org/10.1088/2634-4386/ae45c9/data2.
Tunable regime 1- MEMS 2 available at https://doi.org/10.1088/2634-4386/ae45c9/data3.
Tunable regime 2- MEMS 1 available at https://doi.org/10.1088/2634-4386/ae45c9/data4.
Tunable regime 2- MEMS 2 available at https://doi.org/10.1088/2634-4386/ae45c9/data5.

Conflict of interest

The authors declare that they have no known competing financial interests or personal relationships that could have appeared to influence the work reported in this paper.

Appendix A. Mathematical model

The MEMS resonators are modeled by the dominant mode model, derived and described in [7, 57]. This can be done, since a sound wave can excite without loss of generality only one mode. In general, the model of the MEMS sensor consists of a mechanical and a thermodynamic subsystem combined with a high pass filter:

$$\dot{\boldsymbol{x}}_i = \boldsymbol{f}_i(\boldsymbol{x}_i) = \begin{bmatrix} x_{i,2} \\ -\omega_i^2 x_{i,1} - \frac{\omega_i}{Q_i} x_{i,2} + \alpha_i x_{i,3} + \frac{1}{m} F_{\text{ex}} \\ -\beta_i x_{i,3} + \zeta_i u_{\text{act},i}^2 \\ -\frac{1}{\tau_i} x_{i,4} + \kappa_i x_{i,2} \end{bmatrix}, \tag{A.1a}$$

$$t > 0,\ \boldsymbol{x}_i(0) = \boldsymbol{x}_{0,i},$$

$$y_i = \boldsymbol{h}(\boldsymbol{x}_i) = x_{i,4}, t \geqslant 0. \tag{A.1b}$$

Herein, the states, the controllable voltage, the external input, the output and the initial conditions are denoted by $\boldsymbol{x}_i = [x_{1,i}(t), x_{2,i}(t), x_{3,i}(t), x_{4,i}(t)]^{\mathrm{T}} \in \mathbb{R}^4$, $u_{\text{act},i}(t) \in \mathbb{R}$, $F_{\text{ex}}(t) \in \mathbb{R}$, $y_i(t) \in \mathbb{R}$ and $\boldsymbol{x}_{0,i} \in \mathbb{R}^4$ for all $i = 1, 2$. Thereby, the state vector consists of the deflection $x_{1,i}$ of the beam movement, the velocity $x_{2,i}$ at the free end of the beam, the temperature difference $x_{3,i}$ compared to the environment, and the high-pass filtered deflection signal $x_{4,i}$. The calculation of feedback and coupling is given by

$$u_{\text{act},i} = k_i x_{4,i} + \gamma_{ij} x_{4,j} + u_{\text{DC},i} \tag{A.2}$$

with the feedback strength $k_i \in \mathbb{R}$, the coupling strength $\gamma_{ij} \in \mathbb{R}$ and a bias voltage $u_{\text{DC},i}$ for all $i, j = 1, 2$ and $i \neq j$. Additional parameters are given by the natural frequency $\omega_i = 2\pi f_i > 0$, the Q-factor $Q_i > 0$, the effective mass $m > 0$ of the first mode, the calibration factor $\kappa_i \in \mathbb{R}$, the transfer factors $\alpha_i, \zeta_i > 0$ and the time constants $\beta_i, \tau_i > 0$ for all $i = 1, 2$. The heating efficiency constant ζ_i can be expressed by $\zeta_i = \gamma_i / R_i^2$ with the transfer factor $\gamma > 0$ and the resistance $R > 0$.

Appendix B. Fabrication and design of the MEMS sensor system

The resonators are fabricated on a 4 inch silicon wafer [66]. On this silicon wafer, a layer of siliconoxid (SiOx) is deposited using plasma enhanced chemical vapor deposition. The piezoresistor are deposited using high doped $p{+}{+}$ boron implantation. For actuation, aluminum loops is deposited using magnetron sputtering. The thickness of the resonator is controlled by etching out the back side of the silicon wafer with potassium hydroxide (KOH). For further details regarding the fabrication process please refer to [67]. The MEMS sensors are designed to achieve a high sensitivity for sound. Therefore, they consist of (i) a silicon cantilever with integrated piezoresistive deflection sensing and integrated thermomechanical actuation using an aluminum heater and (ii) of a silicon membrane surrounding the cantilever. For more details regarding to the design considerations see e.g. [7, 68]. The sensor setup is sketched in figure 1(E). The voltage signals from Wheatstone bridge are high passed filtered to remove the DC part of the voltage and then forwarded into the FPGA of Redpitaya STEMLAB-14 board, where feedback and coupling mechanisms are implemented. The actuation voltage $u_{\text{act},i}$ for two sensors is calculated following (A.2). The experimental setup implements three different types of mechanisms: (i) feedback mechanism, (ii) Coupling mechanism, (iii) combination of feedback and coupling mechanism. When the feedback strength k_i or the coupling strength γ_{ij} increase above a critical point, system undergoes an Andronov–Hopf bifurcation. This critical point is denoted by $k_{i,j}^*$ for the feedback critical point for all $i, j = 1, 2$ or $\gamma_{12}^* \gamma_{21}^*$ for the coupling critical point. Signal acquisition as well as generation are implemented in the STEMLAb-14 board using 14 bit, 125MHz ADC and DAC.

Appendix C. Parameters for the mathematical model

The parameters of the investigated MEMS sensors are summarized in table B1. Most of the parameters here are measured using PSV-500 which is a laser doppler vibrometer (LDV) from Polytec GmbH. The

Table B1. Parameters of the MEMS sensors.

			MEMS sensor				
Parameter			1	2	3	4	5
Natural frequency	f	[Hz]	3630	3790	4380	5190	3730
Q-factor	Q		40	80	75	60	70
Calibration factor	κ	$[\frac{\mathrm{V}}{\mathrm{m}}]$	$12.069 \cdot 10^6$	$1.186 \cdot 10^6$	$8.772 \cdot 10^6$	$0.1 \cdot 10^6$	$0.998 \cdot 10^6$
Resistance	R	[Ω]	12.53	12.43	12.33	12.5	12.5
Transfer factor	α	$[\frac{\mathrm{m}^2}{\mathrm{Ks}^2}]$			19.2		
	$\alpha\gamma\kappa$	$[\frac{\mathrm{Vm}}{\mathrm{A}^2\mathrm{Ks}^3}]$	$7.788 \cdot 10^{14}$	$4.631 \cdot 10^{14}$	$1.917 \cdot 10^{14}$	$0.818 \cdot 10^{14}$	$0.644 \cdot 10^{14}$
Time constant	β	$[\frac{1}{\mathrm{s}}]$	150	250	160	60	270
	τ	[s]	$1 \cdot 10^{-3}$				

natural resonance frequency and Q-factor are measured with PSV-500 when the resonators were acoustically excited using frequency chirp. Once the natural resonance frequency was known, resonators were excited acoustically at this single tone frequency. The electrical signal from the piezoresistor was acquired by signal acquistion and generator module of PSV-500. Simultaneously, the deflection is measured and recorded by the LDV. When excited by the signal tone signal, the calibration factor can be obtained by dividing the electrical signal with the deflection signal. The quasi static time constant is measured by exciting the actuation loop of the resonator with signal generator of LDV. Here a 500 mV DC-voltage u_{DC} is given periodically at 1 Hz frequency and deflection x_1 of the signal is measured. From the time series, the rise time of the signal is measured that is 63% of time taken to reach maximum deflection. Taking inverse of this rise time, time constant β is obtained. The resistance R of the resonator is manually measured from PCB using a multimeter. Once the parameters $\omega, x_1, R, u_{\mathrm{DC}}, \beta$ are known the transfer factor $\alpha\gamma$ is calculated using the formula $\alpha\gamma = 4\beta(\pi\omega R)^2 u_{\mathrm{DC}}^{-2} x_1$.

Appendix D. Bifurcation analysis of two coupled MEMS sensors

To explain the observation of the tunable characteristic frequency $f_{\mathrm{C},1}$, the bifurcation analysis of two coupled MEMS sensors was derived in [49] and shortly summarized her(E) for this, the emergence of Andronov–Hopf bifurcations is investigated by determining a bifurcation parameter, which induces one pair of complex conjugated eigenvalues on the imaginary axis at specific values, see, e.g. [69]. Here, the product of the coupling strengths $\gamma_{12}\gamma_{21}$ is the bifurcation parameter. With this, it is demonstrated in [49, section IV] that the critical points of two coupled MEMS sensors are obtained by solving the system of equations

$$0 = q_{11}^2 + q_{12}^2 - q_{21}^2 - q_{22}^2 - \gamma_{12}^*\gamma_{21}^*, \tag{D.1a}$$
$$0 = [b_{11}b_{21}(k_{11} - k_{22} + 2q_{21}) - a_{21}b_{11} + a_{11}b_{21}]\omega_{\mathrm{C}}^2 + (a_{23}b_{11} - a_{13}b_{21})\omega_{\mathrm{C}}^4, \tag{D.1b}$$
$$0 = (b_{11} - b_{21})\omega_{\mathrm{C}}^5 + (a_{12}b_{21} - a_{22}b_{11})\omega_{\mathrm{C}}^3 + 2b_{11}b_{21}q_{12}\omega_{\mathrm{C}}^2 + (a_{20}b_{11} - a_{10}b_{21})\omega_{\mathrm{C}}, \tag{D.1c}$$
$$0 = a_{13}\omega_{\mathrm{C}}^3 + [b_{11}(k_{11} + q_{11} + q_{21}) - a_{11}]\omega_{\mathrm{C}}, \tag{D.1d}$$
$$0 = \omega_{\mathrm{C}}^4 - a_{12}\omega_{\mathrm{C}}^2 - b_{11}(q_{12} + q_{22})\omega_{\mathrm{C}} + a_{10}, \tag{D.1e}$$
$$0 = q_{11}q_{22} - q_{21}q_{12} \tag{D.1f}$$

for the constants $q_{11}, q_{12}, q_{21}, q_{22} \in \mathbb{R}$, the critical point $\gamma_{12}^*\gamma_{21}^* \in \mathbb{R}$, and the characteristic frequency ω_{C}. Additional parameters read

$$a_{i0} = \frac{\beta_i\omega_i^2}{\tau_i}, \qquad a_{i1} = \beta_i\omega_i^2 + \frac{\beta_i\omega_i}{Q_i\tau_i} + \frac{\omega_i^2}{\tau_i}, \qquad a_{i2} = \frac{\beta_i}{\tau_i} + \frac{\beta_i\omega_i}{Q_i} + \frac{\omega_i}{Q_i\tau_i} + \omega_i^2,$$
$$a_{i3} = \beta_i + \frac{\omega_i}{Q_i} + \frac{1}{\tau_i}, \qquad b_{i1} = 2\alpha_i\kappa_i\zeta_i u_{\mathrm{DC},i}$$

for all $i = 1, 2$. By solving (D.1*b*)–(D.1*e*) for q_{11}, q_{12}, q_{22}, and ω_{C} and inserting the result into (D.1*f*), a cubic polynomial (in terms of q_{21}) is obtained. In particular, this implies that two coupled MEMS sensors have three critical point $\gamma_{12,i}^*\gamma_{21,i}^*$ and three corresponding characteristic frequencies $\omega_{\mathrm{C},i}$ for all $i = 1, 2, 3$, which are summarized in [49, appendix C].

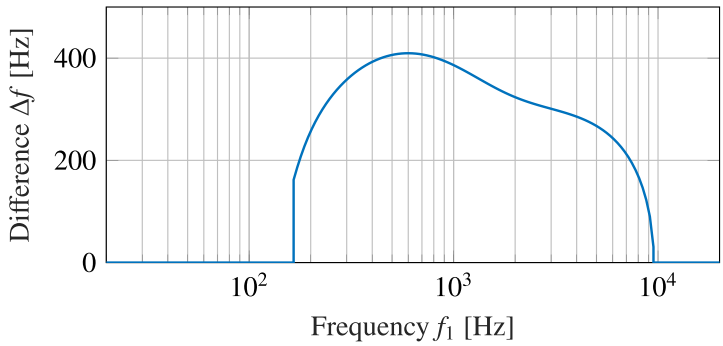

Figure D1. Maximal tunable frequency difference in terms of the natural frequency f_1. The natural frequency is given by $\omega = 2\pi f$. Adapted from [49]. CC BY 4.0.

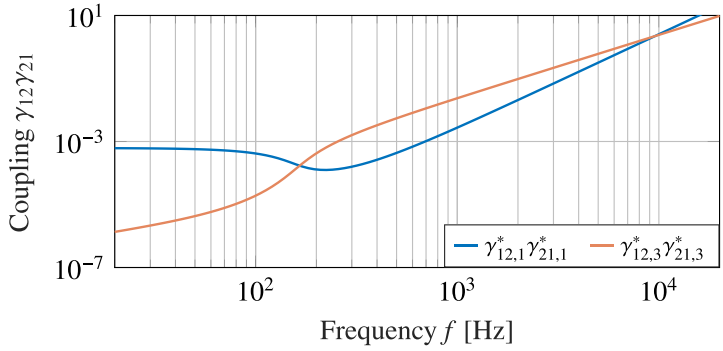

Figure D2. Comparison between the critical coupling points $\gamma^*_{12,1}\gamma^*_{21,1}$ and $\gamma^*_{12,3}\gamma^*_{21,3}$ of the Andronov–Hopf bifurcations responsible for the frequency tunable regime 1 and the untunable regime of two coupled, identical MEMS sensors in terms of the natural frequency f. Adapted from [49]. CC BY 4.0.

As there are multiple critical points, two pairs of complex conjugated eigenvalues can be on the imaginary axis for specific parameter configurations. In particular, this is the necessary condition of an Hopf–Hopf bifurcation, see, e.g. [69], and the bifurcation is used in [49] to determine the frequency difference $\Delta f = |f_1 - f_2|$ at which the dominant bifurcation change. For this, the critical point of the Hopf–Hopf bifurcation between $\gamma^*_{12,1}\gamma^*_{21,1}$ and $\gamma^*_{12,3}\gamma^*_{21,3}$ is computed numerically by solving

$$\gamma^*_{12,1}\gamma^*_{21,1} = \gamma^*_{12,3}\gamma^*_{21,3}$$

for the additional bifurcation parameter Δf. To evaluate the frequency difference Δf inducing the Hopf–Hopf bifurcation, the numerical parameters are given by the Q-factor $Q = 30$, the transfer factor $\alpha\gamma\kappa = 1.022 \times 10^{14}\,\frac{\mathrm{Vm}}{\mathrm{AKs}^3}$, the resistance $R = 12.5\,\Omega$, and the time constants $\beta = 1006.6\,\frac{1}{\mathrm{s}}$ and $\tau = 10^{-3}\,\mathrm{s}$. The frequency difference Δf inducing the Hopf–Hopf bifurcation is visualized in figure D1. Here, the frequency difference Δf can be determined in $[165, 9550]$ Hz, while the critical point cannot be computed outside of $[165, 9550]$ Hz. This behavior can be explained by considering the critical points of the Andronov–Hopf bifurcations responsible for frequency tnable regime 1 and the untunable regime of two coupled, identical MEMS sensors, which is depicted in figure D2. With this, it is showcased that the Andronov–Hopf bifurcation responsible for the frequency tunable regime 1 is dominant in $[165, 9550]$ Hz as $\gamma^*_{12,1}\gamma^*_{21,1} < \gamma^*_{12,3}\gamma^*_{21,3}$.

ORCID iDs

Kalpan Ved 0009-0002-7731-0421
Hermann Folke Johann Rolf 0009-0004-3620-1311
Thomas Meurer 0000-0002-9175-2157
Claudia Lenk 0000-0002-3040-1265

References

[1] Abreu Araujo F *et al* 2020 *Sci. Rep.* **10** 328
[2] Abeßer J 2020 *Appl. Sci.* **10** 2020
[3] Wu J, Yılmaz E, Zhang M, Li H and Tan K C 2020 *Front. Neurosci.* **14** 199
[4] Altoè A and Shera C A 2024 *Phys. Rev. Res.* **6** 013084
[5] Cherry E C 1953 *J. Acoust. Soc. Am.* **25** 975–9
[6] Bronkhorst A W 2000 *Acta Acust. United Acust.* **86** 117–28
[7] Lenk C, Hövel P, Ved K, Durstewitz S, Meurer T, Fritsch T, Männchen A, Küller J, Beer D and Ivanov T 2023 *Nat. Electron.* **6** 1–11
[8] Ammari H and Davies B 2020 *Proc. R. Soc. A* **476** 1471–2946
[9] Rupin M, Lerosey G, De Rosny J and Lemoult F 2019 *New J. Phys.* **21** 093012
[10] Zhao L and Zhou S 2019 *Sensors* **19** 788
[11] Dal Poggetto V F, Bosia F, Urban D, Beoletto P H, Torgersen J, Pugno N M and Gliozzi A S 2023 *Mater. Des.* **227** 111712
[12] Wen B and Boahen K 2009 IEEE transactions on biomedical circuits and systems *Conf. Nam(E) IEEE Trans. on Biomedical Circuits and Systems* vol **3** pp 444–55
[13] Zolfagharinejad M, Büchel J, Cassola L, Kinge S, Syed G S, Sebastian A and van der Wiel W G 2025 *Nature* **645** 1–7
[14] Gold T, Pumphrey R J and Gray J 1948 *Proc. R. Soc. B* **135** 462–91
[15] Gold T and Gray J 1948 *Proc. R. Soc. B* **135** 492–8
[16] Davis H 1983 *Hear. Res.* **9** 79–90
[17] Dallos P 1992 *J. Neurosci.* **12** 4575–85
[18] Weiss T F, Peake W T, Ling A and Holton T 1978 *Which Structures Determine Frequency Selectivity and Tonotopic Organization of Vertebrate Cochlear Nerve Fibers? Evidence From the Alligator Lizard* (*Evoked Electrical Activity in the Auditory Nervous System*) (Academic) pp 91–112
[19] Turner R G, Muraski A A and Nielsen D W 1981 *Science* **213** 1519–21
[20] Weiss T 1982 *Hear. Res.* **7** 353–60
[21] Eguíluz V M, Ospeck M, Choe Y, Hudspeth A J and Magnasco M O 2000 *Phys. Rev. Lett.* **84** 5232–5
[22] Hudspeth A J 1997 *Curr. Opin. Neurobiol.* **7** 480–6
[23] LeMasurier M and Gillespie P G 2005 *Neuron* **48** 403–15
[24] Kern A and Stoop R 2011 *Neural Comput.* **23** 2358–89
[25] De Boer E 1975 *J. Acoust. Soc. Am.* **58** 1030–45
[26] Lyon R F 2011 Using a cascade of asymmetric resonators with fast-acting compression as a cochlear model for machine-hearing applications
[27] Lyon R F 2017 *Human and Machine Hearin(G) Extracting Meaning From Sound* (Cambridge University Press)
[28] Saremi A and Lyon R F 2018 *J. Acoust. Soc. Am.* **143** EL418–24
[29] Duke T and Jülicher F 2003 *Phys. Rev. Lett.* **90** 158101
[30] Ospeck M, Eguíluz V M and Magnasco M O 2001 *Biophys. J.* **80** 2597–607
[31] Kern A and Stoop R 2003 *Phys. Rev. Lett.* **91** 128101
[32] Hudspeth A 2008 *Neuron* **59** 530–45
[33] Hudspeth A, Jülicher F and Martin P 2010 *J. Neurophysiol.* **104** 1219–29
[34] Gomez F, Lorimer T and Stoop R 2016 *Phys. Rev. Lett.* **116** 108101
[35] Magnasco M O 2003 *Phys. Rev. Lett.* **90** 058101
[36] Johnstone B, Patuzzi R and Yates G 1986 *Hear. Res.* **22** 147–53
[37] Gelfand S A 2017 *Hearin(G) An Introduction to Psychological and Physiological Acoustics* (CRC Press)
[38] Kozlov A S, Baumgart J, Risler T, Versteegh C P and Hudspeth A 2011 *Nature* **474** 376–9
[39] Richardson G P and Petit C 2019 *Cold Spring Harb. Perspect. Med.* **9** a033142
[40] Miller K K, Atkinson P, Mendoza K R, ÓMaoiléidigh D and Grillet N 2021 *Front. Cell Dev. Biol.* **9** 742529
[41] Pickles J, Comis S and Osborne M 1984 *Hear. Res.* **15** 103–12
[42] Martin P and Hudspeth A 2021 *Annu. Rev. Condens. Matter Phys.* **12** 29–49
[43] Dierkes K, Lindner B and Jülicher F 2008 *Proc. Natl Acad. Sci.* **105** 18669–74
[44] Köppl C and Manley G A 1993 *Hear. Res.* **71** 157–69
[45] Manley G A, Gallo L and Köppl C 1996 *J. Acoust. Soc. Am.* **99** 1588–603
[46] Vilfan A and Duke T 2008 *Biophys. J.* **95** 4622–30
[47] Rolf H F J and Meurer T 2023 *IFAC-PapersOnLine* **56** 181–6
[48] Lenk C, Ekinci A, Rangelow I W and Gutschmidt S 2018 Active, artificial hair cells for biomimetic sound detection based on active cantilever technology *2018 40th Annual Int. Conf. IEEE Engineering in Medicine and Biology Society (EMBC)* pp 4488–91
[49] Rolf H F J and Meurer T 2024 *Chaos* **34** 103135
[50] Rolf H F J, Feketa P, Schaum A and Meurer T 2025 *Neuromorph. Comput. Eng.* **5** 034007
[51] Syms R R A 1998 *J. Microelectromech. Syst.* **7** 164–71
[52] Lee Y C, Wang L K, Chuang Y C, Hong H C and Chiu Y 2024 *IEEE Sens. Lett.* **8** 1–4
[53] Rolf H F J and Meurer T 2024 *IFAC-PapersOnLine* **58** 66–71
[54] Ved K, Rolf H F J, Ivanov T, Meurer T, Ziegler M and Lenk C 2025 *Hear. Res.* **462** 109260
[55] Reddy J N 2017 *Energy Principles and Variational Methods in Applied Mechanics* (Wiley)
[56] Lenk C, Ivanov T, Gubbi V, Ved K, Ziegler M, Fritsch T, Küller J and Beer D 2022 Fortschritte der Akustik-DAGA202 1–4
[57] Roeser D, Gutschmidt S, Sattel T and Rangelow I W 2016 *J. Microelectromech. Syst.* **25** 78–90

[58] Wiesenfeld K and McNamara B 1985 *Phys. Rev. Lett.* **55** 13
[59] Wiesenfeld K and McNamara B 1986 *Phys. Rev. A* **33** 629
[60] Derighetti B, Ravani M, Stoop R, Meier P, Brun E, Broggi G and Badii R 1986 *Adv. Laser Sci. I* **146** 312–3
[61] Maoiléidigh D O and Hudspeth A 2018 *Physica D* **378** 33–45
[62] Ruggero M A, Rich N C, Recio A, Narayan S S and Robles L 1997 *J. Acoust. Soc. Am.* **101** 2151–63
[63] Zhao H B, Liu L M, Yu N, Zhu Y, Mei L, Chen J and Liang C 2022 *J. Neurophysiol.* **127** 313–27
[64] Wersinger E and Fuchs P A 2011 *Hear. Res.* **279** 1–12
[65] Burwood G, Hakizimana P, Nuttall A L and Fridberger A 2022 *Sci. Adv.* **8** eabq2773
[66] Rangelow I W, Ivanov T, Ahmad A, Kaestner M, Lenk C, Bozchalooi I S, Xia F, Youcef-Toumi K, Holz M and Reum A 2017 *J. Vac. Sci. Technol. B* **35** 06G101
[67] Ivanov T 2004 Piezoresistive cantilevers with an integrated bimorph actuator *PhD Thesis Citeseer*
[68] Khan E, Lenk C, Männchen A, Küller J, Beer D, Gubbi V, Ivanov T and Ziegler M 2023 *Influence of Sensor Design on bio-Inspired, Adaptive Acoustic Sensing* (Deutsche Jahrestagung für Akustik)
[69] Guckenheimer J and Holmes P 2013 *Nonlinear Oscillations, Dynamical Systems and Bifurcations of Vector Fields* vol 42 (Springer)
[70] Ved K and Rolf H F J 2026 Mimicking Cochlear Pre-Processing using Critically Coupled MEMS Sensors *Zenodo* (https://doi.org/10.5281/zenodo.18336535)